SLAC-PUB-14148

A Radiometric All-Sky Infrared Camera (RASICAM) for DES/CTIO

Peter M. Lewis*[a], Howard Rogers[a], Rafe H. Schindler[a]
[a]SLAC National Accelerator Laboratory, P.O. Box 20450, Stanford, CA 94309

ABSTRACT

A novel radiometric all-sky infrared camera [RASICAM] has been constructed to allow automated real-time quantitative assessment of night sky conditions for the Dark Energy Camera [DECam] located on the Blanco Telescope at the Cerro Tololo Inter-American Observatory in Chile. The camera is optimized to detect the position, motion and optical depth of thin, high (8-10km) cirrus clouds and contrails by measuring their apparent temperature above the night sky background. The camera system utilizes a novel wide-field equiresolution catadioptic mirror system that provides sky coverage of 2π azimuth and 14-90° from zenith. Several new technological and design innovations allow the RASICAM system to provide unprecedented cloud detection and IR-based photometricity quantification. The design of the RASICAM system is presented.

Keywords: clouds, infrared camera, equiresolution, DES, DECam, all-sky, thermal imaging

1. INTRODUCTION

All-sky photometricity monitors are utilized at astronomical observatories to determine when conditions are appropriate for observation. These devices typically consist of a wide-angle lens mounted on a CCD camera or a thermal infrared sensor coupled to reflective or refractive optics. At the Cerro Tololo Inter-American Observatory (CTIO) in Chile, the CCD-based Tololo All-Sky Camera (TASCA) has been successfully performing optical monitoring for several years[1]. To complement TASCA—and in conjunction with the planned initiation of the Dark Energy Survey (DES) at the 4.0m Victor M. Blanco Telescope at CTIO[2]—a unique thermal infrared camera system has been designed and will be installed at the observatory later this year. Technological advancements and design innovations permit more flexible and powerful sky monitoring than has been available in any previous system. The requirements and design of RASICAM will be discussed herein.

1.1 The benefits of thermal IR

The traditional method for sky-condition monitoring is subjective, requiring the operator to walk outside and declare the sky clear (or not). Using CCD cameras in optical wavelengths is a great improvement on this method, allowing the operator to evaluate conditions remotely, to rely on quantitative information, and to have access to a database of prior conditions. However, apparent optical sky brightness depends so much on the moon phase, ambient brightness and atmospheric variables that results are often inconsistent[3].

In the 8-13μ mid-IR atmospheric window, clear sky appears cold and clouds appear warm. Additionally, maximum sensitivity to thin, hard-to-detect clouds is achieved by selecting a sub-band in the 10-12μ range which corresponds to nearly perfect atmospheric transmission. The effects of varied atmospheric conditions and variable local light pollution levels that plague optical observations become minimal. Although the interpretation of apparent cloud temperatures as corresponding to a particular optical depth is not straightforward, IR imaging provides the greatest cloud/sky discrimination.

1.2 Thermal IR cloud monitor legacy

Christian Werner pioneered an impressive single-channel thermal IR scanning sky monitor in 1973[4]. Detector technology did not advance sufficiently for implementation in an astronomical observatory until 1994 when the Sloan Digital Sky Survey at Apache Point Observatory (APO) in New Mexico installed a scanning-type all-sky IR sky monitor[5]. More recently, static-view monitors have been used at the MAGNUM Robotic Telescope at Haleakala,

*plewis@slac.stanford.edu; phone 1.650.926.2783

Work supported in part by US Department of Energy contract DE-AC02-76SF00515.

Hawaii[6](as well as other near-clones of that device[7]); at APO in a complete redesign of the earlier system[8, 9]; and at the NASA-operated SLR2000 satellite laser ranging station[10].

Due primarily to limits in technology, each of the extant devices fall short of the potential of mid- IR observations for cloud detection and photometric quantification. Radiometric IR cameras, which return a calibrated temperature for each pixel, have historically been expensive cooled semiconductor devices. Non-radiometric devices—used in the industry mostly for surveillance and classed "volts in, video out" devices—are uncooled, cheaper and mechanically simpler, but require blackbody imaging and careful manual calibration to extract temperature data. Furthermore, usage has been limited to the generation of global or local cloudiness metrics without detailed quantification of seeing conditions.

1.3 Next-generation cloud monitor capabilities

In order to achieve the potential of mid-IR cloud monitoring, the detector system must meet five conditions: (1) radiometric output, (2) all-sky coverage, (3) high sensitivity, (4) self-calibration and (5) flat response across entire field. Additional conditions for specific application at CTIO include (6) low cost, (7) automated operation and low maintenance requirements and (8) seamless integration into existing CTIO computing and physical infrastructure. RASICAM is designed to satisfy all of these conditions, assisted by technological advancements and optical design improvements, to be discussed below in detail.

2. THE PHYSICS

2.1 The background: clear-sky mid-IR emission

A cloudless sky constitutes the background for the cloud signal. The temperature distribution of an ideal background for discriminating thin clouds against a clear sky is (1) very cold, (2) temporally stable and (3) independent of zenith viewing angle. The detector images deep space at an essentially uniform ~3^0K through the atmosphere. An atmospheric constituent in thermal equilibrium will emit strongly in the same wavelength bands it absorbs strongly in, via Kirchoff's law with no reflectivity. Emission within the detector's band will raise the apparent temperature of the clear sky. If the constituent varies in concentration or distribution with weather, season or climate, the clear-sky temperature will change unpredictably. Additionally, more emission will be seen at high zenith viewing angles (larger airmass) than at low angles, leading to a non-uniform temperature distribution. Choosing a band that minimizes atmospheric emission is thus critical.

Given a flat uniform-temperature atmosphere with transmission $\tau_{atm}(\lambda,\theta) = e^{-\delta_{IR}(\lambda)\sec\theta}$ where $\delta_{IR}(\lambda)$ is the IR optical depth[11] and θ represents the zenith viewing angle and a detector spectral sensitivity of $S(\lambda)$, the downwelling radiance by the clear-sky atmosphere at the ground is given by a Line-by-Line Radiative Transfer Model[16] (LBLRTM)

$$R_{atm}^{\downarrow}(\theta) = \int\int_{\tau_{atm}(\lambda,\theta)}^{1} I(T(\tau'),\lambda)\cdot S(\lambda)\, d\tau' d\lambda\,, \tag{1}$$

where $I(T(\tau'),\lambda)$ is the blackbody spectral distribution for temperature $T(\tau')$. Assuming that the atmospheric layer is at a constant temperature (an assumption that will have little effect on the broad conclusions of this section), (1) becomes:

$$R_{atm}^{\downarrow}(\theta) \approx \int\left[1-\tau_{atm}(\lambda,\theta)\right]\cdot I(T,\lambda)\cdot S(\lambda) d\lambda\ . \tag{1.2}$$

The microbolometer detector in RASICAM's FLIR A325 camera converts incident radiation into raw detector counts which are then mapped to temperatures based on short and long term calibrations. The camera applies direct 1:1 mapping from counts to apparent temperature, so minimizing the magnitude and variance of clear-sky radiance will correspondingly minimize the magnitude and variance of the apparent temperature background in camera images.

Figure 1 shows the modeled clear-sky FLIR A325 spectral radiance—the integrand of (1.2)—assuming T=250K and θ= 0°. The three main atmospheric emission features include a large O_3 peak around 9.5μ, an H_2O peak on the low wavelength end as well as a small but uniform all-wavelength H_2O emission contribution, and a large peak toward the

long end due to CO_2. Each of these atmospheric constituents compromises the ideal atmospheric emission profile, which would be zero throughout the camera's band.

To minimize apparent temperature—the first background requirement—the three main peaks must be excluded. Assuming the "optimal band" shown in Figure 1, only H_2O and temperature fluctuations remain as a major contributor to background apparent temperature variations. Atmospheric H_2O can vary greatly on a small time scale, but this cannot be mitigated further within the mid-IR atmospheric window. Any emission in this band is still subject to airmass effects but to a certain degree these effects are predictable.

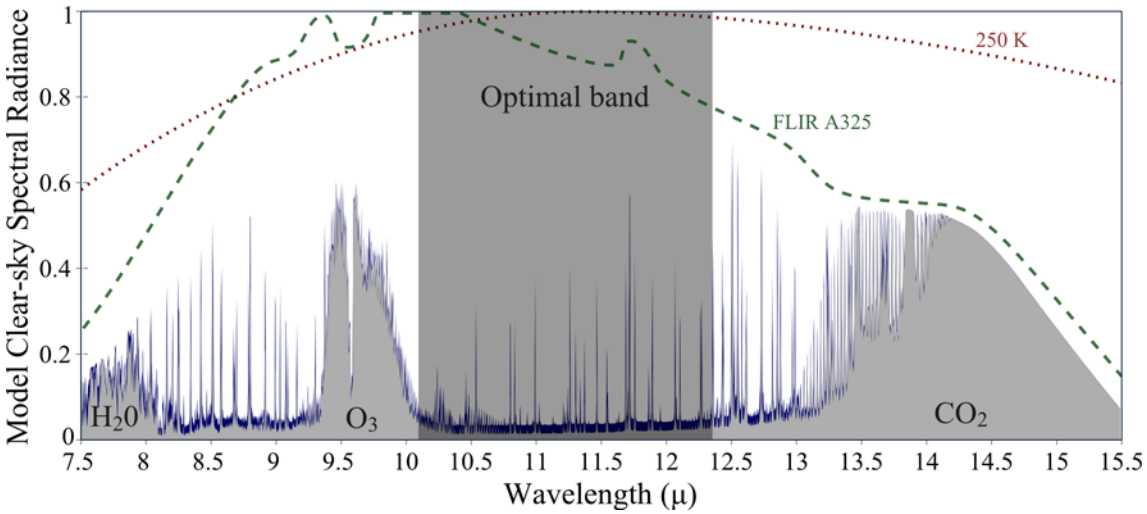

Figure 1. Normalized clear-sky spectral radiance within the FLIR A325 sensitive band. Data is simulated by the ATRAN modeling software[12] for conditions at the Gemini South telescope at Cerro Pachon[13], 10km from CTIO. The light gray area represents emission under an assumed 10mm water vapor column with a relative airmass of 1.0 ($\theta = 0°$). The blue (or dark gray) area represents transmission under 2.3mm water vapor column with the same airmass. The approximate camera spectral sensitivity[14] is overlaid as a dashed gray line, and the blackbody spectrum at 250K is plotted as a dotted line. The shaded region corresponds to the optimal cloud/sky discrimination band. The difference between the 10mm and 2.3mm water vapor column curves illustrates the variability of the transmission with atmospheric moisture content. A similar plot with higher airmass shows increased height for each main emission component. The general form of the plot is insensitive to blackbody temperature.

Sub-ideal but greatly improved background (clear-sky) behavior can thus be achieved by including a bandpass ~10.1-12.4μ filter in the detector optics. Additionally, it appears that water vapor will be the single most important factor compromising the variability of the apparent sky temperature, while the more-predictable airmass effect also raises apparent temperature for large θ.

2.2 The signal: thermal cloud emission

Of primary interest to RASICAM are thin, high cirrus clouds. These clouds are by nature difficult to detect and thus have the highest potential to impact DECam observational data. If a cloud is optically thick [$\tau > 3$] it appears very hot in contrast to the sky and prohibits any kind of observation at all; a binary flag is sufficient to describe the relevant optical properties of a thick cloud.

DeSolver et al.[15] presents a method for extracting visible optical depth from downward IR radiance measurements. A Radiative Transfer Equation (RTE) is constructed assuming a single cloud layer located on top of an emissive atmosphere. The clear atmosphere contribution is equation (1) from LBLRTM without the $S(\lambda)$ factor. The salient results from DeSolver et al. are presented here, with a modification to explicitly denote the contributions from zenith viewing angle θ. The downwelling radiation recorded by a detector with a total spectral sensitivity of $S_{tot}(\lambda)$ is

$$R^{\downarrow}_{tot.}(\theta, p_s, p_b) = \int_{\lambda_{\min}}^{\lambda_{\max}} R^{\downarrow}_{sum}(\lambda, \theta, p_s, p_b) dS_{tot}(\lambda), \quad (2)$$

where $R^{\downarrow}_{sum}(\lambda,\theta,p_s,p_b)$ is a sum of three terms; the downwelling thermal emission from the atmospheric layer below the cloud $R^{\downarrow}_{atm}(\lambda,\theta,p_s,p_b)$, the cloud layer's downwelling thermal emission $R^{\downarrow}_{cloud}(\lambda,\theta,p_s,p_b)$ and upwelling terrestrial thermal emission reflected from the bottom layer of the cloud $R^{\downarrow}_{refl.}(\lambda,\theta,p_s,p_b)$, as given below:

$$R^{\downarrow}_{atm}(\lambda,\theta,p_s,p_b)=\int_{p_b}^{p_s} I[\lambda,T(p)]d\tau_{atm}(\lambda,\theta,p,p_s), \tag{3}$$

$$R^{\downarrow}_{cloud}(\lambda,\theta,p_s,p_b)=\tau_{atm}(\lambda,\theta,p_b,p_s)\int_{p_t}^{p_b} I[\lambda,T(p)]d\tau_{cld}(\lambda,\theta,p,p_b), \tag{4}$$

$$R^{\downarrow}_{refl}(\lambda,\theta,p_s,p_b)=r(\theta)\,\tau_{atm}(\lambda,\theta,p_b,p_s)\,R^{\uparrow}_{terr}(\lambda,\theta,p_s,p_b), \tag{5}$$

with the upwelling terrestrial radiance at the cloud base given by

$$R^{\uparrow}_{terr}(\lambda,\theta,p_s,p_b)=\varepsilon_s\,I[\lambda,T_s]\tau_{atm}(\lambda,\theta,p_s,p_b)+\int_{p_s}^{p_b} I[\lambda,T(p)]d\tau_{atm}(\lambda,\theta,p,p_b). \tag{6}$$

Variables and symbols used in these equations are defined as: p_i for atmospheric pressure at level *i*; *s*, *b*, *t* as labels for surface, cloud base, and cloud top levels respectively; $r(\theta)$ for the reflectivity of the cloud base as a function of viewing angle; and ε_s and T_s for the emissivity and temperature of the terrestrial surface. The model assumes that atmospheric emission inside and above the cloud layer is negligible.

The reflectivity $r(\theta)$is parameterized from data using DeSolver et al[15]. Theory[15], models[17] and experiment[18] confirm that $\delta_{vis}\sim 2\delta_{IR}$, so equation (4) can be rewritten with the replacement $\tau_{cld}(\lambda,\theta,p,p_b)\rightarrow \exp[-\tfrac{1}{2}\delta_{vis}(\lambda,p,p_b)\sec\theta]$, allowing a determination of visible optical depth from IR radiance measurements.

In order to utilize the RTE to extract visual optical depths from radiance measurements, real-time pressure, water vapor content, and temperature profiles are required. Pending observations with RASICAM's camera at the Calypso Observatory on Kitt Peak will help determine if ground level conditions measurements coupled with best-guess look-up-tables and generalizations about cirrus properties are sufficient to accurately construct a visual optical depth map from IR radiance maps.

2.3 Equiresolution

Uniformity—the "flatness" of the detector system response to an extended isotropic signal source—is critical for the optimization of cloud detection in IR. In general, wide-field radially-symmetric catadioptric sensors—mixed lens-and-mirror systems like RASICAM—are not intrinsically uniform, and the nonuniformity will appear as slowly changing temperature bias that depends only on the zenith angle of viewing. This bias perfectly mimics or masks reflection and airmass effects, making uniformity a key component of an optical depth sensor.

Assuming isotropic emission, an infinite plane radiator will appear equally bright for all zenith angles by the definition of a Lambertian radiator. An optical system, however, may partition the incident radiation inequitably between detector pixels. If each pixel imaged the same solid angle (Ω) of sky then the intensity measured by the detector—and thus the inferred temperature of the plane—will be uniform. Such a detector would see no non-atmospheric temperature gradients, giving it the required uniformity for a sensitive cloud monitor.

If the pixel$\rightarrow\Omega$ mapping is constant the optics are called equiresolution. RASICAM's optical design, presented here, makes it the first documented equiresolution IR detector. This property will allow RASICAM to apply temperature-based metrics across the whole sky provided that airmass, reflection and the temporal variability of the atmosphere can be properly accounted for.

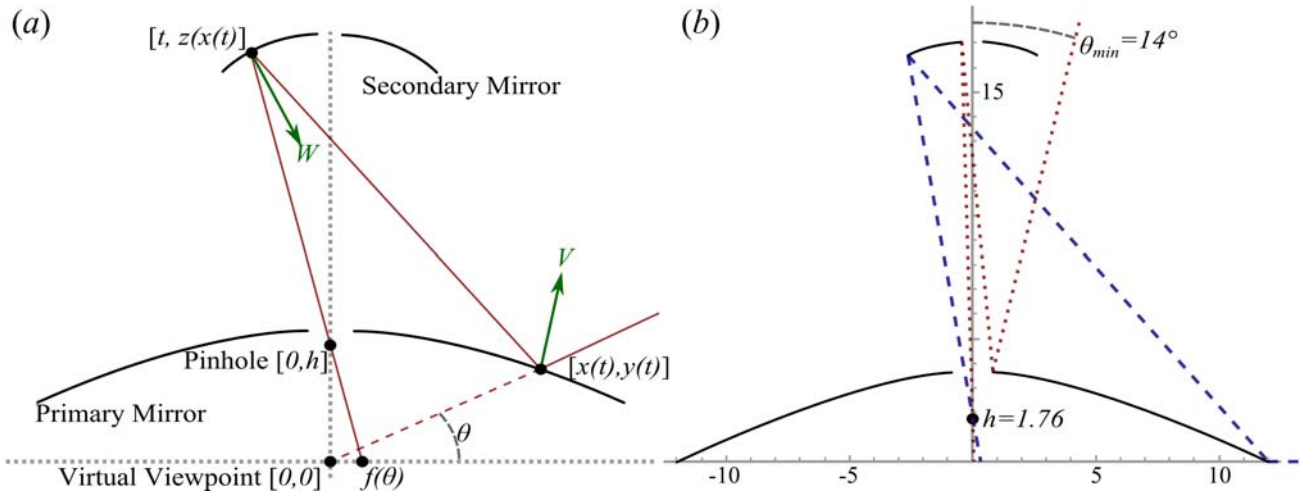

Figure 2. Equiresolution central-projection two-mirror design based on Hicks et al[19]. 2(*a*) shows geometry of general system for a projection *f*. *W* and *V* are the normal vectors for the secondary and primary mirrors, respectively. The extrema of the visible zenith angles are shown. Details are provided in the text. 2(b) shows the actual solution[20] as solved by Mathematica.

2.4 Solving for the optics

Figure 2(*a*) shows the central two-mirror projection geometry[19]. Incident rays at an inclination of θ that are aimed at the virtual viewpoint [*0,0*] are mapped through the pinhole at [*0,h*] onto the location [*f(θ),0*] on the sensor plane. Assuming parameterized mirror profile coordinates *x(t), y(t)* and *z(x(t)),* the tangent to the profile at each solution point is perpendicular to the normal vectors *V* and *W*:

$$[x'(t), y'(t)] \cdot V = 0, \tag{9}$$

$$[1, z'(x(t), y(t))] \cdot W = 0 \tag{10}$$

where geometry gives the normal vector decomposition in terms of the profile coordinates:

$$V = \frac{\{t - x(t), z(t) - y(t)\}}{\sqrt{[t - x(t)]^2 + [z(t) - y(t)]^2}} + \frac{\{x(t), y(t)\}}{\sqrt{x^2(t) + y^2(t)}}, \tag{11}$$

$$W = \frac{\{x(t) - t, y(t) - z(t)\}}{\sqrt{[t - x(t)]^2 + [z(t) - y(t)]^2}} + \frac{\{-t, h - z(t)\}}{\sqrt{t^2 + [h - z(t)]^2}}. \tag{12}$$

The dependent coordinate *z(x(t), y(t))* is taken from geometry, with $\theta(t) = \tan^{-1} y(t)/x(t)$:

$$z(t) = h\left[1 - \frac{t}{f(\theta(t))}\right]. \tag{13}$$

The equiresolution projection[21] is given by

$$f(\theta(t)) = \alpha\sqrt{2\left(1 - \cos\left[\frac{\pi}{2} - \theta(t)\right]\right)} \tag{14}$$

where α is a scale factor that determines the initial height of the secondary. The projection and thus *z(t)* are specified by *x(t)* and *y(t)* only. The dot products in equations (9) and (10) yield a pair of first-order differential equations with considerable symbolic complexity and which are not, in general, analytically solvable.

The mirror profile[20] was solved using Mathematica. For practical uses, Table (1) shows a description of each parameter used to solve the differential equations numerically, as well as considerations for usage in RASICAM.

Table 1. Parameters used in solving for the equiresolution two-mirror central projection profiles. Spatial solution values interpreted in inches; the primary was machined from a 24”x4” aluminum block. See Figure 2(b) for the solution.

Par.	Description	Effect	RASICAM value
t_0	Initial value of “time” parameter	Sets inner radius of secondary; negative values required for solution.	−0.445. Chosen after iterative search to force $x(t_0)$ to match physical requirements.
t_f	Final value of “time” parameter	Sets outer radius of secondary; must be negative	−2.6. Chosen to match secondary physical diameter.
x_0	$x(t_0)$	Sets inner primary radius	Not set (1.865) See above for t_0.
x_f	$x(t_f)$	Sets outer primary radius	12.0”
y_0	$y(t_0)$	Sets maximum thickness of primary	Not set (3.829). Other parameters chosen to keep under 4.0
y_f	$y(t_f)$	Sets max zenith angle seen: $\theta_{\max} = \pi - \tan^{-1}\left[y_f / x_f\right]$	0.0. Chosen to force 90° zenith maximum angle.
α	Standoff parameter.	Sets secondary standoff height. Controls whether f or $-f$ is to be solved.	0.22. Chosen to optimize physical height vs. θ_{min}.
h	Pinhole height above virtual view point—also corresponds to camera lens height.	Directly influences minimum FOV.	$f(\theta(t_f))/\tan(10°) = 1.764$. Chosen to match A325 FOV (18.8°/2) with small clipping.

Raytracing verified that the mirror solutions are indeed equiresolution. The solution assumes, however, that pinhole imaging, which is not necessarily a good model for the camera optics. Raytraces using a full A325 optics model provided by FLIR embedded at the theoretical pinhole location in the mirrors solution were performed. Imaging an infinite Lambertian plane, the modeled detector response differed across all zenith angles indistinguishably from pinhole models. Only pending observations can verify for certain that the pinhole solution is valid for the camera as well, but the raytracing certainly supports this conclusion. Raytracing also revealed that focus optimization will be critical for minimizing distortions to the uniformity profile introduced by severe astigmatism near the horizons.

3. THE HARDWARE

Figure 3 shows a CAD-generated rendering of RASICAM, and Figure 6 shows the system connectivity. Main components include the camera module (Figure 4), mirrors and weather enclosure. The system is designed to be weather-proof without the enclosure, with the enclosure included for robustness. A detailed description of each main component is included.

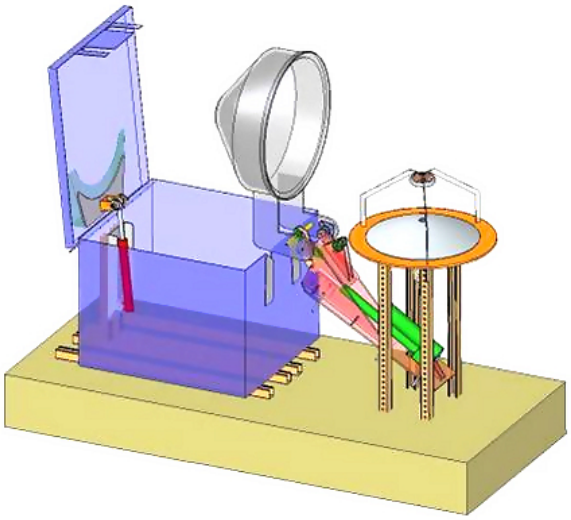

Figure 3. Rendering of RASICAM outdoor hardware, with mirrors, camera module, support structure, and weather enclosure. The weather enclosure is shown mid-way through the process of deploying. For scale, the base is ~3'x8'.

3.1 Camera Module

The camera module includes all of the critical optics and electronics except the mirror. The module is designed to be independently weather-proof and robust enough to be handled and shipped separately without disassembly in order to protect and isolate sensitive components within. Descriptions of each component are included below, using Figure 4 as a reference for labeling.

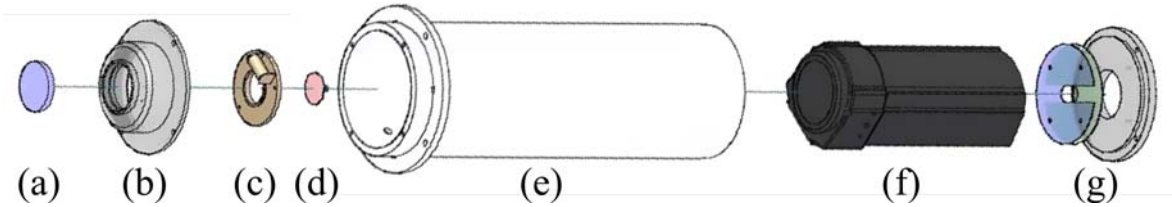

Figure 4. Camera module. The critical optics are embedded in a modular weather-proof shell with the following components (details contained in the text): (a) Ge window, (b) cap, (c) IR calibration shutter, (d) bandpass filter, (e) module shell, (f) FLIR A325 camera and (g) rear weather seal.

The **Germanium window (a)**, from Del Mar Photonics, is a 5mm-thick, 38.1mm-diameter IR-transparent wafer that provides protection for the filter and camera. The front surface of the window has a "diamond-like carbon" coating to protect from weather and abrasions while the back surface has an anti-reflection coating tailored to 8-12μ to minimize contamination from the camera's own IR signature. The window is inset into the module "cap" (b) and sealed for water-tightness.

The **module cap (b)** acts as the interface between the module and the primary mirror. It is a black anodized aluminum fixture that protrudes until the embedded Ge window is flush with the top surface of the middle of the primary.

The **IR calibration shutter (c)** is an electronically-controlled mechanical shutter with a high-emissivity coating on the inside surface, from CVI Melles Griot. A thermocouple is coupled to the shutter to complete the calibrations, and a TTL-

driven circuit is located exterior to the module to operate the shutter—which requires no power to remain open—at the bare-minimum power.

The **bandpass filter (d)**, from the University of Reading Multilayer Laboratory, is a 25.4mm diameter, 3.7mm thick mid-IR bandpass filter on a ZnS substrate. With a center wavelength of 11.13μ and a bandwidth of 2.64μ and an average transmission of ~80%, the filter is nearly perfectly tailored to the mid-IR atmospheric window in exclusion of both the ozone and carbon dioxide peaks.

The **module shell (e)** is an anodized aluminum tube designed to mount directly onto the rear surface of the primary, 8" long and 4" in diameter.

The **FLIR A325 camera (f)** is a mid-IR radiometric microbolometer camera with 320x240 pixels reporting calibrated temperature at 16-bit depth with a maximum frame rate of 60Hz. As a self-calibrating uncooled device, the A325 is much cheaper, more reliable and smaller (exterior dimensions 70x70x170mm) than previous radiometric IR cameras. With an NETD (Noise-Equivalent Thermal Distance) of 50mK, the A325 is not as sensitive as cooled radiometric devices, but given the relatively slow motion of clouds, images can be co-added in real time to significantly improve the effective NETD of the camera while lowering its frame rate. As of purchase, the A325 was the only microbolometer camera on the market with radiometric output. The camera communicates bilaterally with software provided by FLIR over a dedicated gigabit Ethernet cable.

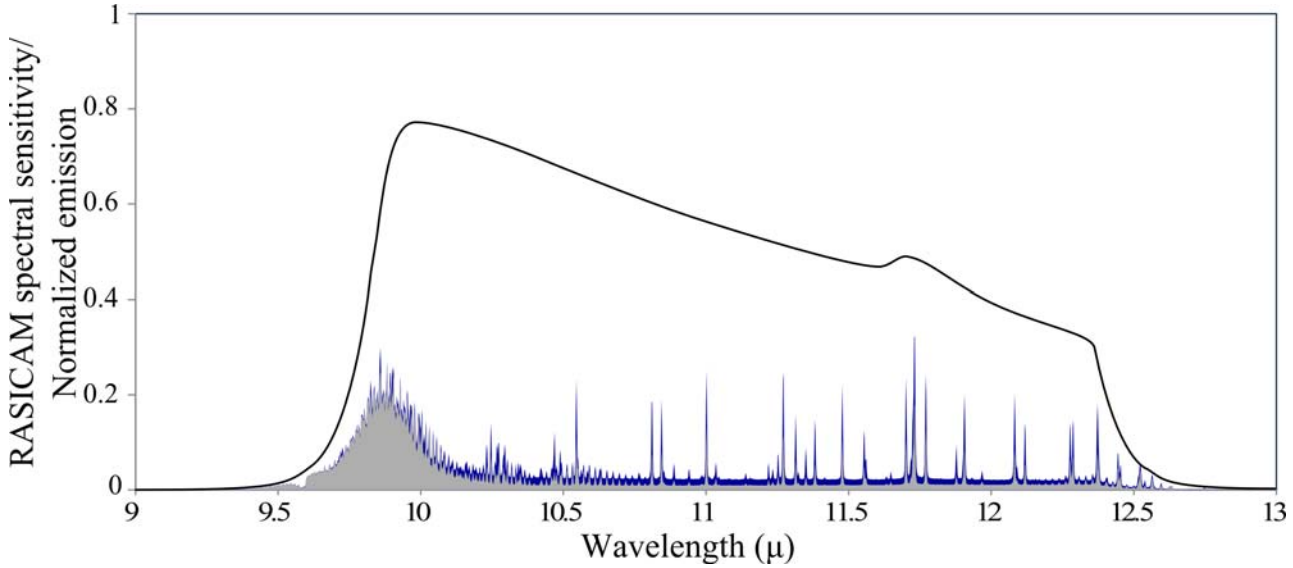

Figure 5. RASICAM total spectral sensitivity $S(\lambda)$ and the normalized clear-sky spectral emission. $S(\lambda)$ is a product of the spectral sensitivity of the A325 camera[14], the spectral transmittances of the Ge window[22] and band pass filter[23] and the reflectivity of the mirror surfaces[24]. The emission spectrum is for a 250^0K blackbody model atmosphere as in Figure 1, multiplied by $S(\lambda)$. Remnants of the ozone peak are passed at the short end, but emission elsewhere is dominated by atmospheric water vapor. Correct characterization of the background components will allow proper response to changing conditions.

The **rear weather seal (g)** permits cables but not water to enter the rear of the module.

3.2 Mirrors

Both mirrors were machined from 6061-T6 aluminum blocks on an NC lathe at Diamond Tools and Die, Inc., located in Oakland, CA from profiles specified by the equiresolution solution. With surfaces specified to 16-32 micro-inches roughness, the mirrors were subsequently polished with a series of diamond pastes to a surface figure of a fraction of a micron. Pre-polishing metrology showed excellent agreement between the cut mirror surface and the specified equiresolution solution.

The primary mirror is ~4" thick and 24" in diameter with substantial volume removed from the underside to reduce weight. The secondary, which sits ~17" above the bottom of the primary, is 5.2" in diameter and nearly 1" thick. The size of the primary was limited mostly by budget and machining constraints.

To enhance reflectivity and protect against oxidation and mechanical damage, the optical surfaces of the mirrors were coated in several layers by EMF Corporation. After surface preparation, a vacuum-deposited gold layer ~120nm thick was topped with ~170nm SiO_2. The gold layer provides excellent mid-IR reflectivity, >99.5% across the bandpass filter[24], and the SiO_2 layer provides scratch-resistance and a cleanable surface.

The effect of the mirror reflectivity coupled with the module optics can be expressed with a single spectral sensitivity curve, seen in Figure 5. Knowing the form of this curve is essential for identifying cirrus emission against a clear-sky background with changing atmospheric conditions.

3.3 Weather enclosure

To shield the device from inclement weather and to cover it during daylight hours, a fiberglass cone will be deployed from a weather-sealed container (see Figure 3). Power, controlling electronics, indicators, and electronic safety measures are included in an enclosure (not pictured) under the primary.

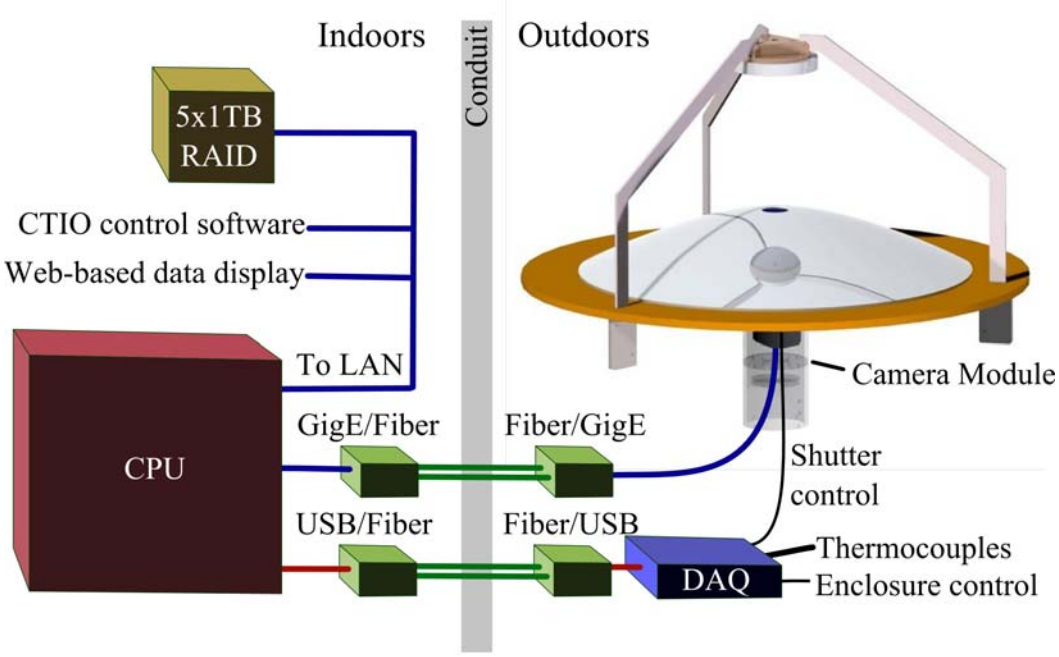

Figure 6. RASICAM connectivity. The CPU and RAID are located indoors and are integrated into local network infrastructure. Connections between the CPU and outdoor hardware components are made through fiber links with corresponding wire/fiber interfaces. The DAQ, located outside, handles all digital I/O duties and reads the thermocouple array as well as controlling the IR calibration shutter. The camera communicates with the CPU via a dedicated gigabit Ethernet line.

3.4 Miscellaneous

Stainless steel tripod legs were designed to support the secondary with minimal cross section and electropolished to minimize emissivity. A ~36" Al primary mounting plate was chrome plated to protect the surface and to minimize emissivity. All external fixtures were prepared to limit degradation and emissivity.

3.5 DAQ

A Cole-Parmer USB data acquisition (DAQ) module, located under the primary (see Figure 6), controls all non-image I/O operations at the outdoor site. In addition to triggering shutter operation and controlling the weather enclosure, the DAQ reads an array of thermocouples to record local temperatures at various locations in and around the device. Thermocouple data will be used to correct measurements, perform calibrations and as a possible input into radiative transfer calculations. The DAQ will also interface with a variety of state sensors.

4. THE SOFTWARE

A LabVIEW virtual instrument is responsible for the automated control of RASICAM. Although a complete description of the code is beyond the scope of this paper, the general function of the software is provided below. Each subsection corresponds to a parallel process implemented in the RASICAM controller software.

4.1 DAQ control

I/O bits and thermocouple values are continually written and monitored according to the current state of the software. Real-time bilateral communication with other parallel modules in the software is required for the calibration operation and for initialization.

4.2 Operator/User display

A web-based interface is used by the operator to monitor current sky conditions and report automated flags and data and to manually override operation of RASICAM. Users—visitors or data users—will have access to the same live data but without controls. The main function of the display is to provide a view of the current temperature distribution in the sky above CTIO along with overlays interpreting the distribution as clear, cirrus or thick clouds. The uniformity of the sky is plotted as a global indicator of clouds, and several automatic flags are generated to indicate general conditions. The past and extrapolated future motion of cloud edges can also be displayed as well as a video of previous frames.

4.3 Core module

The core module handles every aspect of data management, from camera control for acquisition, to processing, display and storing. The module records N frames from the camera as well as the counts→temperature mapping for the current calibration, as a look-up-table (LUT). The N frames are co-added to improve signal significance in real time, while the next batch of frames is capturing. Co-added images are subjected to a variety of conditioning procedures such as flat-fielding to remove detector aberrations and complex scaling to handle current temperature and water vapor conditions as well as to remove the airmass effect. The calibration LUT is applied to the conditioned data to generate a uniform all-sky temperature map of the current sky.

The current sky map is fed into several parallel analysis processes, including cloud identification, thresholding, histogramming and cloud trajectory determination algorithms. Relevant data is saved as a series of overlays that are made available to the operator, with a particular emphasis on conditions near the current target location of the Blanco telescope. Data analysis is heavily parallelized and is complete before the next set of N frames is captured, allowing a zero-frame dead time between captures.

The core module also controls camera internal and external calibrations and is responsible for cataloging events on the hard drive.

4.4 TCP/IP socket

To interact with DES software, a TCP/IP socket is active throughout data-taking. The socket allows the DES software to query specific or local data as well as the real-time automatic conditions data. RASICAM can in turn query for the timestamp and current Blanco targeting coordinates. The potential—as yet unimplemented—is for the DES targeting strategy software to use current and predicted future optical depth and local temperature variation information as a target discrimination metric.

4.5 Miscellaneous

An active right-ascension and declination calculator provides a real-time pixel-location→RA/Dec. mapping to enable correlation of sky conditions with DES data. The mapping is saved as a LUT and associated with a particular series of frames.

A timing module is responsible for looking up sunset and sunrise times and triggering on/off sequences.

ACKNOWLEDGEMENTS

Funding for the DES Projects has been provided by the U.S. Department of Energy, the U.S. National Science Foundation, the Ministry of Science and Education of Spain, the Science and Technology Facilities Council of the United Kingdom, the Higher Education Funding Council for England, the National Center for Supercomputing Applications at the University of Illinois at Urbana-Champaign, the Kavli Institute of Cosmological Physics at the University of Chicago, Financiadora de Estudos e Projetos, Fundação Carlos Chagas Filho de Amparo à Pesquisa do Estado do Rio de Janeiro, Conselho Nacional de Desenvolvimento Científico e Tecnológico and the Ministério da Ciência e Tecnologia, the German Research Foundation-sponsored cluster of excellence "Origin and Structure of the Universe" and the Collaborating Institutions in the Dark Energy Survey.

The Collaborating Institutions are Argonne National Laboratories, the University of California at Santa Cruz, the University of Cambridge, Centro de Investigaciones Energeticas, Medioambientales y Tecnologicas-Madrid, the University of Chicago, University College London, DES-Brazil, Fermilab, the University of Edinburgh, the University of Illinois at Urbana-Champaign, the Institut de Ciencies de l'Espai (IEEC/CSIC), the Institut de Fisica d'Altes Energies, the Lawrence Berkeley National Laboratory, the Ludwig-Maximilians Universität, the University of Michigan, the National Optical Astronomy Observatory, the University of Nottingham, the Ohio State University, the University of Pennsylvania, the University of Portsmouth, SLAC, Stanford University, and the University of Sussex.

Work at SLAC supported by the U.S. Department of Energy under contract number DE-AC02-76SF00515.

Additional thanks to R. Andrew Hicks for help with solving the equiresolution projection, Andrew Rasmussen and Aaron Roodman for assistance with optical ray-tracing and David Burke for optical depth guidance.

REFERENCES

[1] Smith, R., Walker, D. and Schwartz, H. E., "The Tololo all sky camera-TASCA," [Scientific Detectors for Astronomy vol. 300], Springer Netherlands, 379-384 (2004).
[2] Dark Energy Survey Collaboration, "The dark energy survey," AIP Conf. Proc. 842, 989-991 (2006).
[3] Warren, S. G., Hahn, C. J., London, J., "Simultaneous occurrence of different cloud types," J. of Climate and Appl. Meteorology 24, 658-667 (1985).
[4] Werner, C., "Automatic cloud cover indicator system," J. of Applied Meteorology 12(8), 1394-1400 (1973).
[5] Hull, C. L., Limmongkol, S. and Siegmund, W. A., "Sloan digital sky survey cloud scanner," Proc. SPIE 2199, 852-857 (1994).
[6] Saganuma, M., et al., "The infrared cloud monitor for the MAGNUM robotic telescope at Haleakala," Pub. of the Astr. Soc. of the Pacific 119, 567–582 (2007)
[7] Takato, N., et al., "All-sky 10mm cloud monitor on Mauna Kea," Proc. SPIE 4837, 872-877 (2003).
[8] http://irsc.apo.nmsu.edu/irsc_doc/
[9] Anderson, K. S. J., et al., "Apache Point Observatory's all-sky camera: observing clouds in the thermal infrared," Bulletin of the American Astronomical Society 34, 1130 (2002).
[10] Mallama, A., Degnan, J., Cross, F., Mackenzie, J., "Infrared sky camera: the production model," Proc. from the Thirteenth International Workshop on Laser Ranging (2002).
[11] Chamberlain, M. A., Ashley, M. C. B., Burton, M. G., Phillips, A. and Storey, J. W. V., "Mid-infrared observing conditions at the south pole," The Astr. J. 535, 501-511 (2000).
[12] Lord, S. D., "A new software tool for computing Earth's atmospheric transmission of near- and far-infrared radiation," NASA Tech. Memo. 103957 (1992).
[13] http://sciopsedit.gemini.edu/sciops/instruments/gmos/?q=node/10789
[14] Personal correspondence, FLIR Corporation, May 5, 2010.
[15] DeSolver, D. H., Smith, W. L., Piironen, P. K. and Eloranta, E. W., "A methodology for measuring cirrus cloud visible-to-infrared spectral optical depth ratios," J. of Atmo. and Oceanic Tech. 16, 251-262 (1999).
[16] Clough, S. A., Iacono, M. J. and Moncet, J.-L., "Line-by-line calculation of atmospheric fluxes and cooling rates: application to water vapor," J. Geophys. Res. 97, 15761-15785 (1992).

[17] Fu, Q., Liou, K. N., "Parameterization of the radiative properties of cirrus clouds," J. Atmo. Sci. 50(13), 2008-2025 (1993).
[18] Platt, C. M. R., Scott, J. C. and Dilley, A. C., "Remote sounding of high clouds. Part IV: Optical properties of midlatitude and tropical cirrus," J. Atmos. Sci. 44, 729-747 (1987).
[19] Hicks, R. A., Millstone and M., Daniilidiis, K., "Realizing any central projection with a mirror pair," Applied Optics 45(28), 7205-7210 (2006).
[20] http://stanford.edu/~pltrogon/DoubleMirrorProfilePDF4.pdf
[21] Hicks, R. A., Perline, R. K., "Equiresolution catadioptric sensors," Applied Optics 44(29), 6108-6114 (2005).
[22] http://www.dmphotonics.com/GreyhawkOptics/DLCoating_Ge.htm
[23] http://www.reading.ac.uk/nmsruntime/saveasdialog.aspx?lID=30934&sID=129498
[24] http://www.emf-corp.com/custom.html